

Discrete Breathers with Dissipation

S. Flach and A.V. Gorbach

Abstract The interplay between discreteness and nonlinearity leads to the emergence of a new class of nonlinear excitations, viz. discrete breathers. These time-periodic and spatially localized excitations correspond to generic exact solutions of the underlying nonlinear lattice models. Discrete breathers are not confined to certain lattice dimensions, nor are they sensitive to the particular type of nonlinearity in the system. They are usually dynamically and structurally stable and emerge in a variety of physical systems, ranging from lattice vibrations and magnetic excitations in crystals to light propagation in photonic structures and cold atom dynamics in periodic optical traps. Basic properties of discrete breathers, including spatial localization and stability, are briefly discussed in this chapter. Special focus is placed on a subclass of dissipative discrete breathers. Dissipation eliminates extended waves and allows for various resonances of discrete breathers with damped cavity modes. We discuss applications of the discrete breather concept in systems where dissipation is not only unavoidable but essential in order to observe and manipulate discrete breathers, and in order to use them for spectroscopic tools, amongst others.

1 Introduction

This chapter is about localized excitations in spatially extended discrete systems, i.e. lattices. These systems are translationally invariant, implying the absence of disorder and defects. The common expectation – throw a stone into the water of a

S. Flach

Max-Planck-Institut für Physik komplexer Systeme, Nöthnitzer Str. 38, D-01187 Dresden, Germany, flach@mpipks-dresden.mpg.de

A.V. Gorbach

Centre for Photonics and Photonic Materials, Department of Physics, University of Bath, Bath BA2 7AY, UK

Flach, S., Gorbach, A.V.: *Discrete Breathers with Dissipation*. Lect. Notes Phys. **751**, 289–320 (2008)

DOI 10.1007/978-3-540-78217-9_11

© Springer-Verlag Berlin Heidelberg 2008

lake and follow the evolution of the localized surface wave perturbation – is that an initially localized excitation would distribute its energy over the entire system in the course of time. What could stop such a delocalization process? It needs just two ingredients – the above-mentioned discreteness of the system and evolution equations which are nonlinear. As a result, a new paradigm of nonlinear science has recently emerged – the concept of *discrete breathers* (DB), equally labelled *intrinsic localized modes* (ILM) in solid state physics and *discrete solitons* (DS) in nonlinear optics. These exact solutions of a huge variety of underlying nonlinear lattice models are typically characterized by being *time periodic* and *spatially localized*, independent of the actual (assumed to be large) size of the lattice, independent of the spatial dimension of the lattice, mostly independent of the actual choice of nonlinear forces acting on the lattice, and so on. Mastering their mathematical properties in *Hamiltonian* lattices allows us to also include the effects of dissipation, driving and quantization with relative ease, just to name a few important ones. We will especially focus on dissipative discrete breathers.

Nonlinearity is inherent in many systems in nature. Discreteness is common as well – e.g. solids (crystals) and molecules provide a natural underlying lattice, while artificial systems, e.g. those based on Bose–Einstein condensates in optical lattices, Josephson junction networks, optical devices, or micro-mechanical devices, also involve lattice structures. It thus makes perfect sense to understand the mechanisms of localization in nonlinear lattices and to apply that knowledge to various fields of physics, chemistry, biology, and mechanics.

The first report by Ovchinnikov on localized excitations in one-dimensional chains of coupled anharmonic oscillators dates back to 1969 [1]. After a long time span, Sievers and Takeno took the issue up again, considering the famous Fermi–Pasta–Ulam (FPU) chain and obtaining localized excitations, starting from 1988 [2, 3, 4]. From the beginning of the 1990s, a large number of research groups began to study these localized excitations with great mathematical rigour and detail (see, e.g. [5] for a review). Since then, a considerable amount of further mathematical beauty was (and still is being) added to the theory of localized excitations. In addition to this, it is most important to note that, since 1998, experimental studies have been carried out on a large variety of very different systems, demonstrating the fruitfulness of the concept of localization by discreteness and nonlinearity. In the following, we will discuss the basic aspects and some of the more recent developments, including the effect of dissipation.

1.1 Spatial Discreteness and Nonlinearity

Let us study the combined effect of nonlinearity and discreteness on the spatial localization of a discrete breather at a basic level. To do this, we look into the dynamics of a one-dimensional chain of interacting (scalar) oscillators or atoms with the Hamiltonian

$$H = \sum_n \left[\frac{1}{2} p_n^2 + V(x_n) + W(x_n - x_{n-1}) \right]. \tag{1}$$

The integer n marks the lattice site number of a possibly infinite chain, and x_n and p_n are the canonically conjugated coordinate and momentum of a degree of freedom associated with site number n . The on-site potential, V , and the interaction potential, W , satisfy $V'(0) = W'(0) = 0$, $V''(0), W''(0) \geq 0$. This choice ensures that the classical ground state $x_n = p_n = 0$ is a minimum of the energy H . The equations of motion read

$$\dot{x}_n = p_n, \quad \dot{p}_n = -V'(x_n) - W'(x_n - x_{n-1}) + W'(x_{n+1} - x_n). \tag{2}$$

Let us linearize the equations of motion around the classical ground state. We obtain a set of linear coupled differential equations whose solutions are small amplitude plane waves:

$$x_n(t) \sim e^{i(\omega_q t - qn)}, \quad \omega_q^2 = V''(0) + 4W''(0) \sin^2\left(\frac{q}{2}\right). \tag{3}$$

These waves are characterized by a wave number, q , and a corresponding frequency, ω_q . All allowed plane wave frequencies fill a part of the real axis which is called the linear spectrum. Due to the underlying lattice, the frequency ω_q depends periodically on q , and its absolute value has always a *finite upper bound*. The maximum (Debye) frequency of small amplitude waves is $\omega_\pi = \sqrt{V''(0) + 4W''(0)}$. The dispersion relation, ω_q , is shown in Fig. 1. Depending on the choice of the potential

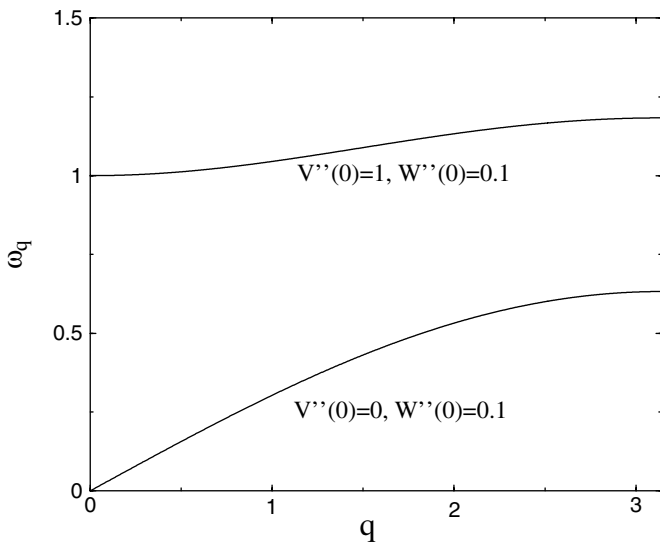


Fig. 1 The dispersion relation for small amplitude plane waves of the model (1)

$V(x)$, it can be either acoustic or optic-like, for $V(0) = 0$ and $V(0) \neq 0$, respectively. In the first case, the linear spectrum covers the interval $-\omega_\pi \leq \omega_q \leq \omega_\pi$, which includes $\omega_{q=0} = 0$. In the latter case, an additional (finite) gap opens for $|\omega_q|$ below the value $\omega_0 = \sqrt{V''(0)}$. Two further characteristics of the linear spectrum are the group velocity, v_g , and the phase velocity, v_{ph} . The group velocity $v_g(q) = d\omega_q/dq$ is a periodic function of q and describes the propagation speed of a wave packet centred at q . At the edge of the linear spectrum, $v_g = 0$. Otherwise its absolute value has a finite upper bound. The phase velocity $v_{ph} = \omega_q/q$ is a non-periodic oscillating function of q . It covers the whole real axis for an optic-like linear spectrum, since $\omega_{q=0} \neq 0$. Its absolute value has a finite upper bound, $|v_{ph}| \leq v_g(q=0)$, for acoustic-like linear spectra.

For large amplitude excitations, the linearization of the equations of motion is no longer correct. As in the case of a single anharmonic oscillator, the frequency of possible time-periodic excitations will depend on the amplitude of the excitation and thus may be located outside the linear spectrum. Let us assume that a time-periodic and spatially localized state, i.e. a *discrete breather*, $\hat{x}_n(t + T_b) = \hat{x}_n(t)$ exists as an exact solution of (2) with the period $T_b = 2\pi/\Omega_b$. Due to its time periodicity, we can expand $\hat{x}_n(t)$ into a Fourier series:

$$x_n(t) = \sum_k A_{kn} e^{ik\Omega_b t}. \quad (4)$$

The Fourier coefficients are, by assumption, also localized in space:

$$A_{k,|n| \rightarrow \infty} \rightarrow 0. \quad (5)$$

Inserting this ansatz into the equations of motion (2) and linearizing the resulting algebraic equations for Fourier coefficients in the spatial breather tails (where the amplitudes are, by assumption, small), we arrive at the following linear algebraic equations:

$$k^2 \Omega_b^2 A_{kn} = V''(0) A_{kn} + W''(0) (2A_{kn} - A_{k,n-1} - A_{k,n+1}). \quad (6)$$

If $k\Omega_b = \omega_q$, the solution of (6) is $A_{k,n} = c_1 e^{iqn} + c_2 e^{-iqn}$. Any non-zero (however small) amplitude $A_{k,n}$ will thus oscillate without further spatial decay, contradicting the initial assumption. However, if

$$k^2 \Omega_b^2 \neq \omega_q^2 \quad (7)$$

for any integer k , then the general solution of (6) is given by $A_{k,n} = c_1 \kappa^n + c_2 \kappa^{-n}$, where κ is a real number which depends on ω_q , Ω_b , and k . It always admits an (actually exponential) spatial decay by choosing either c_1 or c_2 to be non-zero. In order to satisfy (7) for at least one real value of Ω_b and any integer k , we require that $|\omega_q|$ be bounded from above. This is precisely the reason why the spatial lattice is needed. In contrast, most spatially continuous field equations will have linear spectra which are unbounded. Then, resonances of higher-order harmonics of a localized excitation with the linear spectrum become unavoidable. The non-resonance condition (7)

is thus an (almost) necessary condition for obtaining a time-periodic localized state on a Hamiltonian lattice [6, 7].

The existing analysis can be extended to more general classes of discrete lattices, including, e.g. long-range interactions between sites, more degrees of freedom per site, and higher-dimensional lattices. But the resulting non-resonance condition (7) maintains its generality, illustrating the key role of discreteness and nonlinearity for the existence of discrete breathers.

As with any rule, the non-resonance condition may also have exceptions. However, as with any exception, there is a price to pay. When staying within the class of spatially continuous Hamiltonian systems, the price is imposing additional symmetries. While that may be of particular interest for a given application, the additional symmetries usually restrict the richness of possible solutions. And losing the symmetries leads to a loss of localized excitations – in contrast to the nonlinear lattice case, where no further symmetries are required.

While the nonlinear lattice appears to be a natural mathematical path to avoid resonances with plane waves which occur in spatially continuous nonlinear Hamiltonian field equations, there are other ways things can evolve. If resonances with plane waves are an obstacle, then we either remove the resonances or simply remove the plane waves! The first possibility can be realized by using a lattice, or restricting ourselves to equations which either do not contain linear terms or where at least the linear interaction terms vanish, making the linear spectrum degenerate – no matter whether for a lattice or a continuum. The second possibility – removing the plane waves – can be achieved by considering dissipative systems. Indeed dissipation will prevent the persistence of plane waves travelling over infinite distances. Thus, delocalization by itself is then not a problem. The loss of energy inside a breather core due to dissipation has to be taken care of by properly pumping more energy into the breather. We will discuss examples and note that a recently rapidly developing branch of *dissipative solitons* appears to follow exactly this latter path.

1.2 Why Only Time-Periodic Orbits?

In the previous section, we demonstrated how the interplay between nonlinearity and discreteness supports time-periodic and spatially localized solutions, i.e. discrete breathers. What can we say about the existence of more general types of localized solutions with dynamical behaviour which is not time periodic? An analogous approach shows that for a quasi-periodic DB with N incommensurate frequencies $\{\Omega_1, \Omega_2, \dots, \Omega_N\}$, the non-resonance condition (7) transforms into [7]

$$\{k_1\Omega_1 + k_2\Omega_2 + \dots + k_N\Omega_N\}^2 \neq \omega_q^2, \quad (8)$$

with k_i being arbitrary integers. In other words, none of the principal frequencies $\{\Omega_1, \Omega_2, \dots, \Omega_N\}$ nor any linear combination of their multiples should resonate with the linear spectrum. However, any incommensurate pair of frequencies Ω_1 and Ω_2 ,

with irrational ratio Ω_1/Ω_2 , will generate an infinite number of pairs k_1, k_2 which violate the non-resonance condition (8) [7]. Therefore, in general, quasi-periodic DBs are not expected to exist as exact spatially localized solutions.

Another question concerns the possibility of existence of moving DBs. A rather general definition of a moving DB assumes a localized object which translates n sites in a certain direction after m periods of internal oscillations, with the ratio n/m being irrational in general. In a one-dimensional chain, such a moving DB corresponds to a solution of (2) with the form

$$x_n(t) = \phi(\xi, t), \quad \xi = n - Vt, \quad (9)$$

$$\phi(\xi, t + T_b) = \phi(\xi, t), \quad \phi(\xi \rightarrow \pm\infty, t) \rightarrow 0. \quad (10)$$

A detailed analysis of possible resonances has been carried out in [8, 9]. It follows that one has to avoid resonances of the velocity V with *phase velocities* v_{ph} of small amplitude plane waves (where the linear spectra which have been modified, as compared with the original underlying one). The essence is that these resonances cannot be avoided, so that moving DBs are not expected to be exact solutions for a general nonlinear lattice. Hence, moving DBs face the obstacle of resonances with phase velocities of plane waves. By removing the plane waves (e.g. by adding dissipation) we can again try to escape from the above-mentioned resonances and construct quasi-periodic DBs and even moving DBs.

1.3 Examples of Discrete Breather Solutions

Let us now present discrete breather solutions for various lattices. We start with a chain (1) with the functions

$$V(x) = x^2 + x^3 + \frac{1}{4}x^4, \quad W(x) = 0.1x^2. \quad (11)$$

The spectrum, ω_q , is optic-like and is shown in Fig. 2. Discrete breather solutions can have frequencies Ω_b which are located either below or above the linear spectrum. The time-reversal symmetry of (2) allows us to search for DB displacements, $x_n(t = 0)$, when all velocities $\dot{x}_n(t = 0)$ are zero. These initial displacements are computed with high accuracy and plotted in the insets in Fig. 2 [10]. We show solutions for two DB frequencies located above and below ω_q – their actual values are marked with the green arrows. For each DB frequency, we show two different spatial DB patterns among an infinite number of other possibilities. The high-frequency DBs ($\Omega_b \approx 1.66$) occur for large-amplitude, high-energy motion, with adjacent particles moving out of phase. Low-frequency DBs ($\Omega_b \approx 1.26$) occur for small-amplitude motion, with adjacent particles moving in phase.

In Fig. 3, we show two DB solutions for a Fermi–Pasta–Ulam chain of particles coupled via anharmonic springs, $V(x) = 0, W(x) = \frac{1}{2}x^2 + \frac{1}{4}x^4$ (cf. (1)) which is of acoustic type [11]. The DB frequency in both cases is $\Omega_b = 4.5$. Again, the

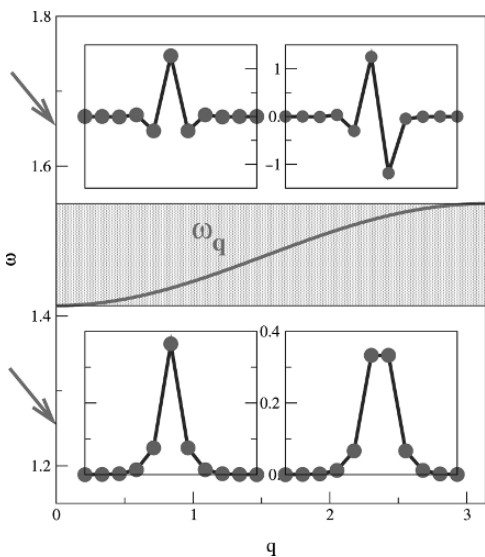


Fig. 2 The frequency versus wave-number dependence of the linear spectrum for a one-dimensional chain of anharmonic oscillators with potentials (11). The chosen DB frequencies are marked with green arrows and they lie outside the linear spectrum, ω_q . Red circles indicate the oscillator displacements for a given DB solution, with all velocities equal to zero. Lines connecting circles are guides for visualization (Figure adapted from [10])

displacements x_n are shown for an initial time when all velocities vanish. In the inset, we plot the strain $u_n = x_n - x_{n-1}$ on a log-normal scale. The DB solutions are exponentially localized in space.

Finally, we show DB solutions for a *two-dimensional* square lattice of anharmonic oscillators with nearest-neighbour coupling. The equations of motion read

$$\ddot{x}_{i,j} = k(x_{i+1,j} + x_{i-1,j} - 2x_{i,j}) + k(x_{i,j+1} + x_{i,j-1} - 2x_{i,j}) - x_{i,j} - x_{i,j}^3 \quad (12)$$

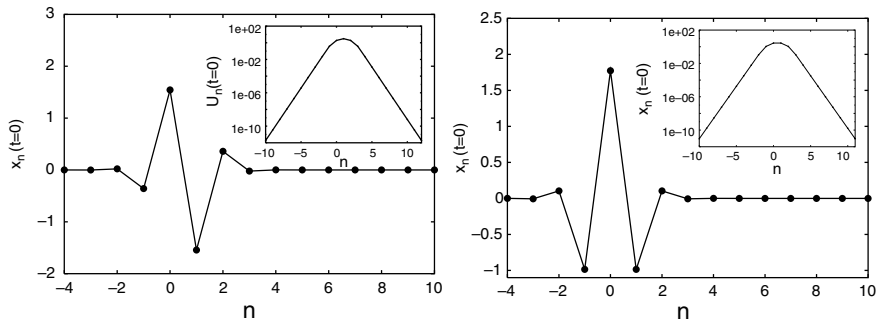


Fig. 3 Discrete breather solutions for a Fermi-Pasta-Ulam chain (see text) (Figure adapted from [11])

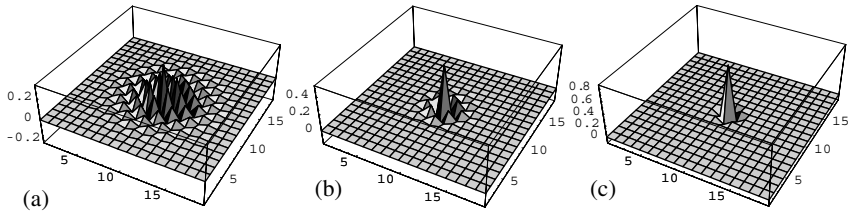


Fig. 4 Displacements of DBs on a two-dimensional lattice (12) with $k = 0.05$, with all velocities equal to zero. (a) $\Omega_b = 1.188$; (b) $\Omega_b = 1.207$; (c) $\Omega_b = 1.319$ (Figure adapted from [12])

which corresponds to oscillator potentials $V(x) = \frac{1}{2}x^2 + \frac{1}{4}x^4$. In Fig. 4, we plot the oscillator displacements with all velocities equal to zero for three different DB frequencies and $k = 0.05$ [12]. Adjacent oscillators move out of phase for all these cases.

We conclude this section by emphasizing that DB solutions can typically be localized on a few lattice sites, regardless of the lattice dimension. Thus, little overall coherence is needed to excite a state nearby – just a few sites have to oscillate coherently, while the rest of the lattice does not participate strongly in the excitation.

2 Basic Properties of Discrete Breathers

2.1 Spatial Localization

Discrete breathers are generic solutions on nonlinear lattices. As for their localization properties in space, we can consider both the profile inside the core of the DB and the decay properties in its spatial tails. The former aspect is the hardest one, since it needs mastery of the full nonlinear equations. The latter one is more accessible since breather amplitudes become small in their tails. A linearization of the equations of motion in the tails is then usually expected to correctly describe the tail asymptotics. Furthermore, one can even systematically go beyond such a linearization and treat nonlinear corrections as well.

To be specific, we will consider a model with one degree of freedom per unit cell. Generalizations to more complicated cases should be straightforward. The Hamiltonian reads

$$H = \sum_l \left[\frac{1}{2} P_l^2 + V(X_l) + \sum_{l'} W_{l,l'}(X_l - X_{l'}) \right]. \quad (13)$$

The hyper-cubic lattice has dimension d , and the lattice index l is a d -dimensional vector with integer components. The interaction potential $W_{l,l'} = W_{l+m,l'+m}$, and hence the model, is translationally invariant. All zero and first derivatives of the

potential functions vanish for zero arguments. By the virtue of the discreteness, the frequency spectrum, ω_q , of small amplitude plane waves is bounded in absolute value.

A discrete breather solution is given by

$$X_l(t) = \sum_k A_{kl} e^{ik\Omega_b t}. \tag{14}$$

Here the Fourier number, k , is a scalar integer which is independent of the lattice dimension, d . The breather is localized in space, which implies

$$A_{k,|l| \rightarrow \infty} \rightarrow 0. \tag{15}$$

Assuming that the potential functions have non-zero second derivatives at their origin, i.e. $V''(0) = v_2 \neq 0$ and $W''_{0,l} = w_{0,l} \neq 0$ for some l , we may try to linearize the algebraic equations for the Fourier coefficients A_{kl} :

$$k^2 \Omega_b^2 A_{kl} = v_2 A_{kl} + \sum_{l'} w_{l,l'} (A_{kl} - A_{kl'}). \tag{16}$$

Since the Fourier amplitude equations decouple after linearization, we can solve each of these equations on its own. Recalling that the necessary condition for the possible localization of each Fourier amplitude is the non-resonance condition $k\Omega_b \neq \omega_q$, the spatial decay of the k th amplitude is then given by the lattice Green's function [13]

$$G_\lambda(l) = \int_{1.BZ} \frac{\cos(ql)}{\omega_q^2 - \lambda} d^d q, \quad \lambda = k^2 \Omega_b^2. \tag{17}$$

Here, the integration extends over the first Brillouin zone of the reciprocal wave-number space, q . We note that the spectrum, ω_q , is periodic in q , with its irreducible multi-dimensional period residing exactly in the first Brillouin zone. Fixing the direction of l and changing its absolute value, (17) will then generate the Fourier coefficients of the periodic function $(\omega_q^2 - \lambda)^{-1}$. The spatial decay of the breather is thus characterized by the convergence properties of the corresponding Fourier series, and the convergence properties of the Fourier series are defined through the analytical properties of the corresponding periodic function.

We describe a lattice as having short-range interactions if the corresponding squared spectrum, ω_q^2 , is an analytic function on the extended wave-vector space q , i.e. where all its derivatives, at any point q , exist and are finite. Examples are lattices with nearest-neighbour interactions, and more general lattices with finite-size interactions where $w_{0,l} = 0$ for $|l| > r$, with r being a positive real number. However, we can even generalize this by considering lattices where the harmonic interaction potential extends over the whole lattice, with exponentially decaying amplitudes [14] $w_{0,l} \sim e^{-|l|/r}$ for $|l| \gg r$. For all these cases, the denominator $(\omega_q^2 - \lambda)^{-1}$, which appears in (17), is an analytic periodic function of q , and thus the convergence of its Fourier series and the spatial localization of a DB are bound by exponential tails [15]. The exponent will depend on $\lambda = k^2 \Omega_b^2$. The localization length will grow whenever any of the multiples $k\Omega_b$ come close to an edge of the spectrum ω_q .

In the insets in Fig. 3, the exponentially localized profiles of two DBs are shown for a one-dimensional FPU chain with nearest-neighbour interaction. A comparison between the numerically obtained localization length and the prediction from (17) has been made for various one-dimensional lattices in [7, 16] and is discussed extensively in [5].

Here, we also present the amplitude distribution of a DB solution for a three-dimensional cubic DNLS lattice with nearest-neighbour interaction:

$$\dot{\Psi}_l = i(\Psi_l + |\Psi_l|^2\Psi_l + 0.1 \sum_{m \in N_l} \Psi_m), \quad (18)$$

where N_l denotes the set of nearest neighbours of l . On making the substitution $\Psi_l = A_l e^{i\Omega_b t}$, the algebraic equations are solved for the real amplitudes A_l [17] for a lattice with size 31^3 . To visualize the solution, we place the DB centre at the lattice site $l = (16, 16, 16)$ and plot its amplitude distribution as a function of the (x, y) coordinates in a plane with fixed coordinate $z = 16$, which contains the lattice site with the maximum breather amplitude. Note that the DB is strongly localized on a few lattice sites (see left plot in Fig. 5). The same solution, when displayed on a logarithmic amplitude scale, shows a conical structure (see right plot in Fig. 5), as expected from the predicted exponential decay in space.

We describe a lattice as having long-range interactions if the corresponding squared spectrum, ω_q^2 , is a non-analytic function on the extended wave-vector space q , i.e. some of its derivatives, at some points q , diverge or do not exist. That happens, for example, when a harmonic interaction potential extends over the whole lattice and decays algebraically with increasing distance $w_{0,l} \sim |l|^{-s}$, with some positive exponent, s . Despite the slow decay of interactions, discrete breathers still exist, but now their localization will be slower than exponential. In fact, what matters is

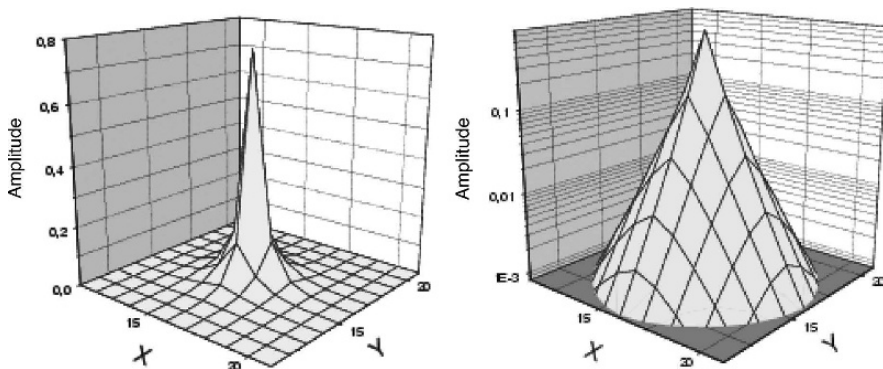


Fig. 5 Amplitude distribution of a breather solution of the three-dimensional DNLS system (18) with size $N = 31^3$. Actually, only a distribution in a cross-section (x, y) plane is shown. (Here, the plane cuts the centre of the breather.) The intersections of the grid lines correspond to the actual amplitudes, while the rest of the grid lines are only guides for visualization. *Left panel* – amplitudes are shown on a linear scale. *Right panel* – the same solution with amplitudes plotted on a logarithmic scale. Data are from Fig. 2 in [17]

the analysis of the degree of non-analyticity of ω_g^2 , which straightforwardly gives a power-law convergence of the Fourier series (17) (see [15]), and thus an algebraic spatial localization of DBs. As shown in [18], more complicated spatial decay laws apply, with crossovers from exponential to algebraic decay.

In the case of a purely nonlinear interaction [7, 19, 20, 21, 22, 23, 24, 25], the spatial decay of a breather is super-exponential, e.g.

$$\ln |\ln |A_n|| \approx n \ln(2m - 1). \tag{19}$$

Such solutions are also called quasi-compact.

Other studies concern resonances with Goldstone modes [26] and nonlinear corrections [16].

2.2 Dynamical Stability of Perturbed Discrete Breathers

Once a DB solution is found, an important question arises regarding its stability. One has to study the problem of evolution of a perturbation, $\epsilon_n(t)$, added to the DB solution, $\hat{x}_n(t)$. If the perturbation amplitude is large enough, one may expect generic dynamical features of a non-integrable system, which are usually rather complicated and hard to address analytically. However, by imposing certain restrictions on the size of perturbation, one may linearize the resulting equations for $\epsilon_n(t)$ [27, 28]:

$$\ddot{\epsilon}_n = - \sum_m \frac{\partial^2 H}{\partial x_m \partial x_n} \Big|_{\{\hat{x}_l(t)\}} \epsilon_m, \tag{20}$$

where H is the Hamiltonian of the system. Within the linear approximation in the perturbation amplitude $\epsilon_n(t)$, the DB acts as a parametric time-periodic driver, and the problem (20) corresponds to a time-dependent Hamiltonian, $\tilde{H}(t)$:

$$\tilde{H}(t) = \sum_n \left[\frac{\pi_n^2}{2} + \frac{1}{2} \sum_m \frac{\partial^2 H}{\partial x_n \partial x_m} \Big|_{\{\hat{x}_l(t)\}} \epsilon_n \epsilon_m \right], \tag{21}$$

$$\dot{\epsilon}_n = \frac{\partial \tilde{H}}{\partial \pi_n}, \quad \dot{\pi}_n = - \frac{\partial \tilde{H}}{\partial \epsilon_n}. \tag{22}$$

The specific structure of the Hamiltonian, \tilde{H} , ensures the conservation law $\dot{I} = 0$ [27, 29] for the symplectic product

$$I = \sum_n [\epsilon_n(t) \pi'_n(t) - \epsilon'_n(t) \pi_n(t)] \tag{23}$$

of any two trajectories $y = \{\epsilon_n, \pi_n\}$ and $y' = \{\epsilon'_n, \pi'_n\}$. It can be written as the scalar product

$$I = (Jy, y'), \quad (24)$$

where J is the $2N \times 2N$ matrix

$$J = \begin{pmatrix} 0 & I \\ -I & 0 \end{pmatrix}, \quad (25)$$

and I is the $N \times N$ unit matrix. The conservation of the symplectic product I implies that the evolution matrix, $U(t)$, which maps the linearized phase space flow around the given periodic orbit (corresponding to the DB solution) onto itself

$$\begin{Bmatrix} \varepsilon(t) \\ \pi(t) \end{Bmatrix} = U(t) \begin{Bmatrix} \varepsilon(0) \\ \pi(0) \end{Bmatrix}, \quad (26)$$

is symplectic:

$$U^T J U = J. \quad (27)$$

Due to the time periodicity of all the coefficients on the right-hand side of (20), the dynamics of the small-amplitude perturbation $\varepsilon_n(t)$ is fully determined by the Floquet matrix $\mathcal{F} \equiv U(T_b)$, i.e. by the evolution matrix over the DB period, T_b . Thus, the problem is reduced to the determination of eigenvalues and eigenvectors of the symplectic Floquet matrix \mathcal{F} .

The condition of linear (marginal) stability of the DB solution is that all perturbations remain bounded in time. This implies that all the Floquet eigenvalues λ_v are located on the unit circle in the complex plane: $|\lambda_v| = 1$ (see Fig. 6, left picture).

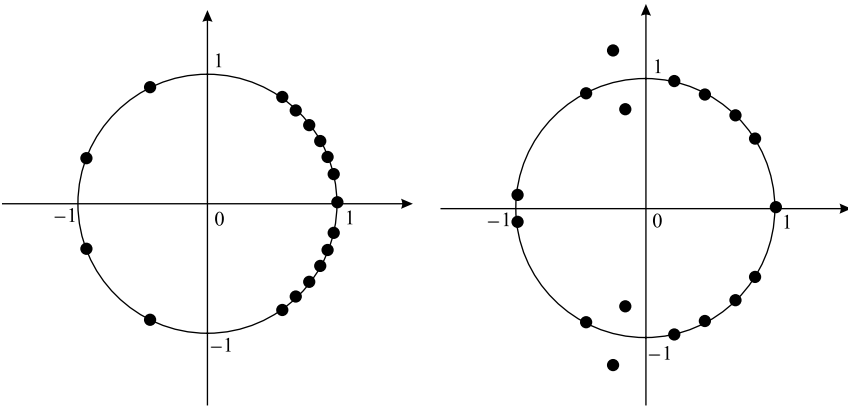


Fig. 6 Schematic view of an outcome of the Floquet analysis of a breather in a Hamiltonian system, Floquet eigenvalues (*filled circles*), and the unit circle in the complex plane. *Left picture*: stable breather (all eigenvalues are located on the unit circle). *Right picture*: unstable breather (two pairs of eigenvalues have collided on the unit circle, and one eigenvalue per pair departs outside it). Note that the group of eigenvalues in proximity on the unit circle correspond to the plane wave continuum (extended Floquet eigenstates), while the separated eigenvalues on the unit circle correspond to localized Floquet eigenstates

All Floquet eigenvalues for a typical DB solution can be divided into two groups, depending on whether the eigenvectors are spatially localized or spatially extended (over the lattice). Since the DB is exponentially localized in a finite region of the lattice, the extended eigenvectors are locally deformed linear modes (standing waves) of the system. Their number is proportional to the size of the system. In contrast, the number of eigenvalues, corresponding to spatially localized perturbations (internal modes of the DB), depends solely on the DB parameters and is finite, even for infinite system size.

For Hamiltonian systems, there are always two isolated eigenvalues, located at $+1$, which correspond to localized Floquet modes [27, 8] – the phase mode describing a rotation of the overall phase of the breather (i.e. sliding along the periodic orbit in phase space) and the growth mode describing a change of DB frequency/energy (i.e. sliding along the DB family).

On changing the model parameters, as well as the DB solution parameter (its frequency or energy), the Floquet eigenvalues will move in the complex plane. However, the only way a particular eigenvalue can leave the unit circle is through a collision with another eigenvalue (see Fig. 6, right picture). To conclude this discussion, the details of the scenario of switching between linearly stable and unstable DB states can be quite complicated. While that may seem a strange complication of the rather straightforward picture of the emergence of DB solutions, it is a consequence of the fact that we deal with periodic orbits in a high-dimensional phase space of non-integrable systems.

2.3 Energy Thresholds of Discrete Breathers

DB solutions come in one-parameter families. The parameter can be the amplitude (measured at the site with maximum amplitude), the energy, E , or the breather frequency, Ω_b . The amplitude can be decreased to arbitrarily small values, at least for some of the families in an infinite lattice. In this zero-amplitude limit, the DB frequency, Ω_b , approaches an edge of the phonon spectrum, ω_q . This happens because the non-resonance condition, $\omega_q/\Omega_b \neq 0, 1, 2, 3, \dots$, has to hold for all solutions of a generic DB family. In the limit of zero amplitude, the DB solutions have to approach solutions of the linearized equations of motion, so the frequency Ω_b has to approach some ω_q , but at the same time it must not coincide with any phonon frequency. This is possible only if the breather's frequency tends to an edge, ω_E , of the phonon spectrum in the limit of zero breather amplitude. If we consider the family of nonlinear plane waves which yields the corresponding band edge plane wave in the limit of zero amplitude A , then its frequency, ω , will depend on A as

$$|\omega - \omega_E| \sim A^z \quad (28)$$

for small A , where the detuning exponent, z , depends on the type of nonlinearity of the Hamiltonian (13) and can be calculated using standard perturbation theory [30].

Here we closely follow the line of argument of [17]. Let us assume that we have a system with short-range interactions and estimate the discrete breather energy in the limit of small amplitudes. Define the amplitude of a DB to be the largest of the amplitudes of the oscillations over the lattice. Denote it by A_0 , where we define the site $l = 0$ to be the one with the largest amplitude. The amplitudes decay in space away from the breather centre, and by linearizing around the equilibrium state and making a continuum approximation, the decay is found to be given by $A_l \sim CF_d(|l|\delta)$ for $|l|$ large, where F_d is a dimension-dependent function:

$$F_1(x) = e^{-x}, \quad F_3(x) = \frac{1}{x}e^{-x}, \quad (29)$$

$$F_2(x) = \int \frac{e^{-x\sqrt{1+\zeta^2}}}{\sqrt{1+\zeta^2}} d\zeta, \quad (30)$$

δ is a spatial decay exponent, and we shall assume that the constant C is of order A_0 . To estimate the dependence of the spatial decay exponent, δ , on the frequency of the time-periodic motion, Ω_b (which is close to the edge of the linear spectrum), it is sufficient to consider the dependence of the frequency of the phonon spectrum, ω_q , on the wave vector, q , close to the edge. Generically, this dependence is quadratic ($\omega_E - \omega_q \sim |q - q_E|^2$, where $\omega_E \neq 0$ marks the frequency of the edge of the linear spectrum and q_E is the corresponding edge wave vector). Then analytical continuation of $(q - q_E)$ to $i(q - q_E)$ yields a quadratic dependence, $|\Omega_b - \omega_E| \sim \delta^2$. Finally, we must insert the manner in which the detuning of the breather frequency from the edge of the linear spectrum, $|\Omega_b - \omega_E|$, depends on the small breather amplitude. If we assume that the frequency of the weakly localized breather detunes with amplitude as the weakly nonlinear band edge plane wave frequency, then this is $|\Omega_b - \omega_E| \sim A_0^z$. Then $\delta \sim A_0^{z/2}$.

Now we are able to calculate the scaling of the energy of the discrete breather as its amplitude goes to zero by replacing the sum over the lattice sites by an integral:

$$E_b \sim \frac{1}{2}C^2 \int r^{d-1} F_d^2(\delta r) dr \sim A_0^{(4-zd)/2}. \quad (31)$$

This is possible if the breather persists for small amplitudes and is slowly varying in space. We find that, if $d > d_c = 4/z$, the breather energy diverges for small amplitudes, whereas for $d < d_c$, the DB energy tends to zero with the amplitude. Inserting $z = 2$, we obtain $d_c = 2$, which is in accord with the exact results on plane wave stability [31], and thus strengthens the conjecture that discrete breathers bifurcate through tangent bifurcations from band edge plane waves. Note that, for $d = d_c$, logarithmic corrections may apply to (31), and these can lead to additional variations of the energy for small amplitudes.

An immediate consequence is that if $d \geq d_c$, the energy of a breather is bounded and is not zero. This is because for any non-zero amplitude, the breather energy cannot be zero, and as the amplitude goes to zero, the energy approaches a positive limit

($d = d_c$) or diverges ($d > d_c$). Thus, we obtain an energy threshold for the creation of DBs for $d \geq d_c$. This new energy scale is set by combinations of the expansion coefficients in (13). We assume $z = 2$ with $|\Omega - \omega_E| \sim \beta A^2$ for the nonlinear plane waves and that the energy per oscillator $E \sim gA^2$. Then the relation $|\Omega_b - \omega_E| \sim \kappa \delta^2$ applies for the spatial decay exponent, δ . Furthermore, the energy threshold, E_{\min} , is of the order of $\kappa g / \beta$, and the minimum energy breather in three dimension has a spatial size which is of the order of the lattice spacing and is independent of κ, g , and β . One should allow for a factor of $(2 + d)$ for underestimating the true height of the minimum and the contributions of nearest neighbours.

Many numerical results have since confirmed the above results. For the d -dimensional DNLS model (18), the left panel in Fig. 7 shows the variation of the DB energy with its central amplitude, and a clear notion of an energy threshold, starting with $d = 2$ [17]. Note that $n = 1$ in that case. The minimum energy DB profile for $d = 3$ is the one plotted in Fig. 5; it is indeed strongly localized on the lattice. It was also observed that energy thresholds even appear in one-dimensional systems, if the lowest-order nonlinear term in the equations of motion has a large enough power. We present results for a modified DNLS system in one spatial dimension, $d = 1$:

$$\dot{\Psi}_l = i \left(\Psi_l + |\Psi_l|^{\mu-1} \Psi_l + C \sum_{m \in N_l} \Psi_m \right). \tag{32}$$

By tuning μ , we can cross over from zero to non-zero energy thresholds. We show results for $d = 1$ and $\mu = 3, 5, 7$ in the right panel of Fig. 7. Again, we find full agreement with the predictions from above. Thus, even one-dimensional lattices

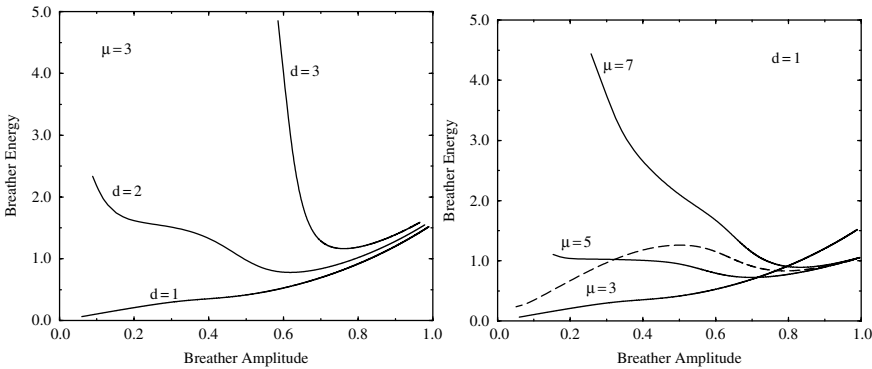


Fig. 7 *Left panel:* Breather energy versus amplitude for the DNLS system in one, two, and three lattice dimensions. System sizes for $d = 1, 2, 3$: $N = 100, N = 25^2$, and $N = 31^3$, respectively. *Right panel:* Breather energy versus maximum amplitude for the DNLS system in one lattice dimension for three different exponent values: $\mu = 3, 5, 7$ (solid lines). The system size is $N = 100$ and the parameter $C = 0.1$. The dashed line is for the modified system (cf. text) (Figure adapted from [17])

exhibit positive lower bounds on breather energies if $\mu \geq 5$. Weinstein has obtained rigorous proofs of these results for any value of μ [32].

We can predict that a modified DNLS system with an additional term $v_{\mu'} |\Psi_l|^{\mu'-1} \Psi_l$ will exhibit complex curves $E_b(A_0)$. For example, for $d = 1$, $\mu = 7$, $\mu' = 3$, and $v_{\mu'} = 0.1$, the $E_b(A_0)$ -dependence will be nearly identical to the case $v_{\mu'} = 0$ already considered, if the amplitude A_0 is not too small. Then $E_b(A_0)$ will show a minimum at a non-zero value of A_0 . For small A_0 , however, the energy of the breather will ultimately decay to zero, so the curve has a maximum for smaller amplitudes! The dashed line in the right panel in Fig. 7 shows the numerical calculation, which coincides with our prediction.

Another example is a two-dimensional lattice system (12) where $d = 2$ is the critical dimension. The energy thresholds have been computed and reported in [12]. The profiles of DB solutions in Fig. 4 correspond to (A) a low-amplitude DB, (B) the minimum energy DB, and (C) a high-amplitude DB.

2.4 Dissipative Discrete Breathers

So far we have been discussing breathers in Hamiltonian lattices. However, any experiment will show up with some dissipation. When this dissipation is of a fluctuating nature, it can be simulated using a heat bath. However, it is also possible to consider simple deterministic extensions to the above problems. In Josephson junction systems, this is actually even implemented experimentally. Let us mention the basic new features one is faced with when studying dissipative breathers and their properties [22, 33, 34].

2.4.1 Obtaining Dissipative Breathes

Consider the following set of equations of motion:

$$\ddot{x}_l = -\frac{\partial H}{\partial x_l} - \gamma \dot{x}_l - I, \quad (33)$$

with

$$H = \sum_l [1 - \cos x_l - C(1 - \cos(x_l - x_{l-1}))]. \quad (34)$$

For $\gamma = I = 0$, this system is Hamiltonian and it corresponds to the Takeno–Peyrard model of coupled pendula [22, 35]. This model allows for the usual discrete breathers, and also for the so-called ‘roto-breathers’. Now $x_l(t + T_b) = x_l(t)$ for all l for a usual breather, but for the simplest version of a roto-breather, one pendulum performs rotations:

$$x_0(t + T_b) = x_0(t) + 2\pi m. \quad (35)$$

Here m is a winding number characterizing the roto-breather (again the simplest realization is $m = 1$). Note that, in contrast to a usual breather ($m = 0$), roto-breathers are not invariant under time reversal.

For non-zero γ and $I = 0$, the non-zero dissipation will lead to a decay of all breather and roto-breather solutions. However, for a time-independent $I \neq 0$, roto-breathers may still exist. The reason is that the rotating pendulum will both gain energy due to the non-zero torque, I , and dissipate energy due to the non-zero friction, γ , so an energy balance is possible (whereas this is impossible for breathers with $m = 0$).

Instead of families of breather periodic orbits in Hamiltonian systems, dissipative roto-breathers will be attractors in the phase space. Attractors are characterized by a finite-volume basin of attraction surrounding them. Any trajectory which starts inside this basin will ultimately be attracted by the roto-breather. Thus, dissipative breathers form a countable set of solutions.

To compute such a dissipative roto-breather, we can simply make a good guess for the initial conditions and then integrate the equations of motion until the roto-breather is reached. This method is very simple, but may suffer from long transient times and also from complicated structures of the boundaries of the basin of attraction.

The Newton method can be applied here as well. Although we do not know the precise period of the roto-breather, we do not actually need it. Instead of defining a map which integrates the phase space over a given time, T_b , we may define a map which integrates the phase space of all but the rotating pendulum coordinate from the initial value $x_0(t = 0) = 0$ to $x_0(t_{\text{map}}) = 2\pi m$. Different trajectories will have different values of t_{map} , but this is not a problem. The only two things we have to worry about are finding a trajectory which leads to a rotation of x_0 and, as usual, being sufficiently close to the desired solution for the Newton map to converge. Once the solution is found, $T_b = t_{\text{map}}$.

2.4.2 Perturbing Dissipative Breathers

If a dissipative roto-breather is stable, then the volume of its basin of attraction is finite, so small deviations will return the perturbed trajectory back to the breather. Upon a change of some control parameter, the breather may still persist but become unstable. Consider the linearized phase space flow around a roto-breather of (33, 34):

$$\dot{\tilde{\epsilon}}_l = - \sum_m \frac{\partial^2 H}{\partial x_l \partial x_m} \Big|_{\{x_l(t)\}} \epsilon_m - \gamma \dot{\tilde{\epsilon}}_l. \quad (36)$$

In analogy with Sect. 2.2, we may introduce a (quasi-symplectic) matrix \mathcal{R} which maps the phase space of the perturbations onto itself by integration of (36) over one breather period [34]. By using the transformation

$$\epsilon_l(t) = e^{-\frac{1}{2}\gamma t} \kappa_l(t), \quad (37)$$

we obtain

$$\ddot{\kappa}_l = - \sum_m \frac{\partial^2 H}{\partial x_l \partial x_m} \Big|_{\{x_l(t)\}} \kappa_m - \frac{1}{4} \gamma^2 \kappa_l. \tag{38}$$

Equation (38) defines a Floquet problem with a symplectic matrix \mathcal{F} with the properties discussed above. By transforming back to \mathcal{R} , we find that those eigenvalues which are located on the unit circle for \mathcal{F} now reside on a circle with a smaller radius

$$R(\gamma) = e^{-\gamma T_b/2}. \tag{39}$$

If μ is an eigenvalue of \mathcal{R} , then so are

$$\mu^*, e^{-\gamma T_b} \frac{1}{\mu}, e^{-\gamma T_b} \frac{1}{\mu^*}. \tag{40}$$

There is still one eigenvalue, $\mu = 1$, which corresponds to perturbations tangent to the breather orbit. The related second eigenvalue is located at $e^{-\gamma T_b}$, in contrast to the Hamiltonian case. A schematic outcome of a Floquet analysis of a dissipative breather is shown in Fig. 8. We close by noting that the above properties of the quasi-symplectic matrix \mathcal{R} follow directly from (36), and thus apply to many other situations in the study of the stability of periodic orbits in dissipative systems.

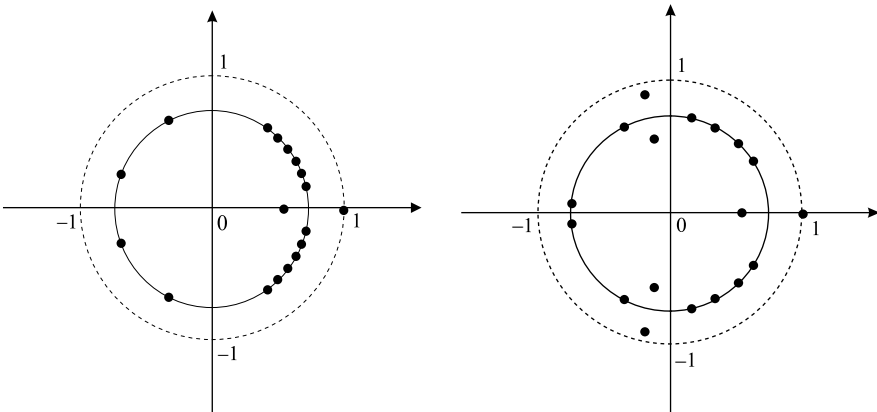


Fig. 8 Schematic view of an outcome of the Floquet analysis of a dissipative breather. Floquet eigenvalues (*filled circles*), the unit circle (*large radius*), and the inner circle of radius R (39) are plotted in the complex plane. *Left picture*: stable breather (all eigenvalues are located on the circle with radius R). *Right picture*: stable breather close to instability (two eigenvalues have collided on the inner circle, and one is departing outside towards the unit circle). Note that the group of eigenvalues in proximity on the unit circle correspond to the plane wave continuum (extended Floquet eigenstates), while the separated eigenvalues on the inner circle correspond to localized Floquet eigenstates

3 Applications

In the following, we will discuss in detail two recent applications of the concept of discrete breathers in systems where dissipation is not only unavoidable but essential in order to observe and manipulate DBs in a way which is impossible for a conservative case.

3.1 Josephson Junction Networks

Arrays of Josephson junctions are perfect laboratory objects to study various nonlinear phenomena. An anisotropic ladder of dc-biased Josephson junctions, as shown in Fig. 9, is perhaps the simplest structure which supports discrete breathers. The dynamics of a single Josephson junction is described by the time evolution of the difference of the phases of the wave function between adjacent superconducting islands, ϕ . It may support two stable states – a superconducting state and a resistive state. In the superconducting state, the average value of $\dot{\phi}$ vanishes. In the resistive state, it is non-zero and proportional to the voltage drop across the junction.

3.1.1 Basic Principles and Modelling

We denote the phase differences across the l th vertical junction and its right upper and lower horizontal neighbours by $\phi_l^v, \phi_l^h, \tilde{\phi}_l^h$. Then, the dimensionless equation of motion for each junction, with current I_l flowing through it, is given by the Josephson equation with its phase difference ϕ_l :

$$\ddot{\phi}_l + \alpha \dot{\phi}_l + \sin \phi_l = I_l. \tag{41}$$

The time is normalized to $t_0 = \sqrt{C\Phi_0/(2\pi I_c)}$, with Φ_0 being a magnetic flux quantum, C the capacitance, and I_c the critical current of the corresponding junction.

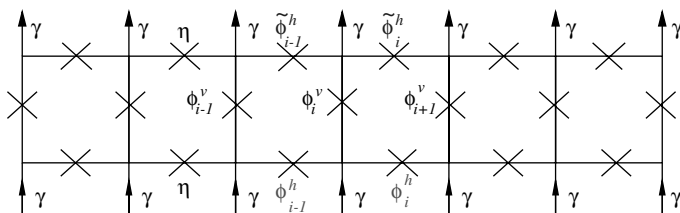


Fig. 9 A schematic view of a Josephson junction ladder (JLL). *Crosses* indicate the locations of junctions, while the *arrows* show the direction of external current flow, γ

The dimensionless damping parameter is $\alpha = \sqrt{\Phi_0/(2\pi I_c C R_N^2)}$ (where R_N is the junction resistance) and $\eta = I_{cH}/I_{cV}$ is the anisotropy constant, i.e. the ratio of the critical horizontal and vertical currents. Note that, due to the sin term, for a resistive junction $\phi = \Omega t + g(t)$, where the zero mean periodic function $g(t) = g(t + 2\pi/\Omega)$ describes periodic modulations of the resistive state. This a.c. Josephson effect also imposes a corresponding oscillation on nearby coupled junctions, which, when time-averaged, are in the superconducting state.

Using the Kirchhoff laws and the self-inductance relation for one elementary cell of the ladder (see [36]), one arrives at the following set of equations:

$$\begin{aligned}\ddot{\phi}_l^v + \alpha \dot{\phi}_l^v + \sin \phi_l^v &= \gamma + (\Delta \phi_l^v - \nabla \tilde{\phi}_{l-1}^h + \nabla \phi_{l-1}^h)/\beta_L, \\ \ddot{\phi}_l^h + \alpha \dot{\phi}_l^h + \sin \phi_l^h &= -(\phi_l^h - \tilde{\phi}_l^h + \nabla \phi_l^v)/(\eta \beta_L), \\ \ddot{\tilde{\phi}}_l^h + \alpha \dot{\tilde{\phi}}_l^h + \sin \tilde{\phi}_l^h &= (\phi_l^h - \tilde{\phi}_l^h + \nabla \phi_l^v)/(\eta \beta_L),\end{aligned}\quad (42)$$

where γ is the dimensionless d.c. bias in units of I_{cV} , $\beta_L = 2\pi L I_{cV}/\Phi_0$ is the dimensionless discreteness parameter, and L is the self-inductance of the elementary cell of the ladder. The discrete operators are given by $\nabla \phi_l = \phi_{l+1} - \phi_l$, $\Delta \phi_l = \phi_{l+1} - 2\phi_l + \phi_{l-1}$. The dispersion law for the plasmon plane waves for the weakly damped case ($\alpha \ll 1$) can be obtained by omitting the damping and linearizing the system (42):

$$\omega_0^2 = 1, \quad \omega_{\pm}^2 = \frac{1}{2} \left[1 + \xi \pm \sqrt{(1 - \xi)^2 + 8(1 - \sqrt{1 - \gamma^2})/(\eta \beta_L)} \right],$$

where $\xi = \sqrt{1 - \gamma^2} + 2[1 + \eta(1 - \cos q)]/(\eta \beta_L)$. The branch ω_0 corresponds to non-active vertical junctions and in-phase (symmetric) oscillations of the phases of upper and lower horizontal junctions. The branch $\omega_+ > \omega_0$ is characterized by anti-symmetric oscillations of the horizontal phases for all qs . For $q = 0$, only the horizontal junctions are excited. The branch $\omega_- < \omega_0$ becomes dispersionless for $\gamma = 0$. For $q = 0$, it corresponds to the excitation of only the vertical junctions, while the horizontal ones are not active.

For a finite-size ladder with open boundary conditions and N cells, i.e. $N + 1$ vertical junctions, the spectrum of linear waves is discrete and is characterized by the following choice of allowed wave-number values:

$$q_l = \frac{l\pi}{N+1}, \quad l = 0, 1, 2, \dots, N. \quad (43)$$

These plasmon waves are the *cavity modes* of the JJJ. Odd values of l correspond to anti-symmetric eigenvectors (with respect to reflections at the centre of the ladder), whereas even values correspond to symmetric ones.

3.1.2 Roto-Breather Solutions and Their Current–Voltage Dependencies

The breather states (roto-breathers in this case) correspond to a few junctions being in the resistive state, with all other junctions oscillating around the superconducting state. These oscillations are induced by coupling to the resistive junctions.

Experiments [37, 38] have revealed different breather structures, as depicted in Fig. 10: (a) up–down symmetry, (b) left–right symmetry, (c) inversion symmetry, (d) no symmetry. Each group of breathers can also have an arbitrary number, n_r , of vertical resistive junctions. Experimentally, each discrete breather is characterized by its current–voltage dependence [37]. Such a time-averaged measurement does not resolve the details of the oscillatory dynamics of a state. This is almost impossible to do, due to the absence of spectroscopic tools at plasma frequencies of the order of 100 GHz. The average voltage drop on the l th vertical junction equals $V = (1/T_b) \int_0^{T_b} \phi_l^y dt$. For the type (a, d) breathers, $V = 2\omega_b$, while for the type (b, c), $V = \omega_b$.

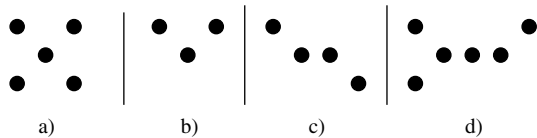
Using the approximation $\phi \sim t$ for resistive junctions, one can compute the dependence of the average voltage drop on the d.c. bias:

$$V = \frac{k\gamma}{\alpha[k + (3 - \frac{1}{2}\delta)\eta]}, \tag{44}$$

where k is the number of vertical rotating junctions and δ denotes the number of resistive horizontal junctions. Note that $\delta = 4$ for breathers with up–down symmetry, $\delta = 2$ for left–right or inversion symmetry, and $\delta = 3$ for no symmetry. Numerical calculations of the current–voltage characteristics (Fig. 11) showed very good qualitative agreement with experiments. In addition, numerical studies allow us to directly access the tricky details of the nonlinear dynamics of the obtained states. Note that the variation of the parameters allows for breathers with frequencies located above the entire plasmon spectrum, as well as in its gaps.

The presence of dissipation leads to a temporal decay of plasmon waves, if excited homogeneously in the ladder. In addition, it also leads to a spatial decay of plasmon waves if a local resonant source is generating them. Thus, a roto-breather in the JjL can be brought into resonance with plasmon waves. The tuning parameter is simply the d.c. bias, which is the main control parameter in the experiments. When the breather frequency is tuned into resonance, the breather starts to generate plasmons, which will localize in space. Their localization length, though finite, will grow with decreasing dissipation constant, α . In a finite ladder, one expects to observe a resonant breather tail, which extends to the end of the ladder, and appears

Fig. 10 Possible realizations of discrete breathers in a linear ladder. *Black spots* indicate the positions of resistive junctions. Ladders with periodic boundary conditions do not support (c) or (d) states



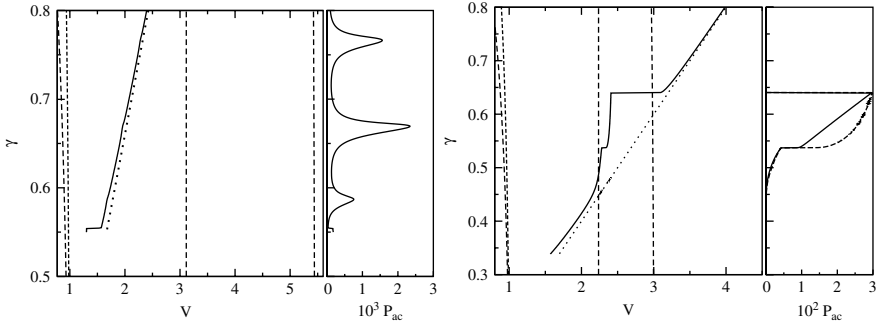


Fig. 11 Current–voltage dependence and the edge average power $P_{ac} = \frac{1}{2} \langle \dot{\phi}_N^2 \rangle$ dependence for breathers of type (b) in a ladder with $N = 10$ vertical Josephson junctions. *Solid lines* – numerical results. *Dotted lines* – approximation (44). *Vertical dashed lines* – band edges of the plasmon wave spectrum. *Left picture* – $\alpha = 0.1$, $\beta_L = 0.2$, $\eta = 1.15$. *Right picture* – $\alpha = 0.1$, $\beta_L = 1.0$, $\eta = 0.5$ (Figure adapted from [36])

at discrete values of the bias, due to the discrete set of cavity mode frequencies. This indeed can be observed, e.g. in the left picture in Fig. 11, where the cavity modes resonate with the second harmonics of the breather frequency. At the same time, almost no indication for that resonance is observable in the current–voltage characteristics.

In the right picture in Fig. 11, the breather frequency itself resonates with the plasmon waves. Still, the breather survives, due to the presence of dissipation. However, the resonant breather–plasmon interaction is now strong, and this leads to a considerable change in the current–voltage characteristics. Almost vertical resonant steps are observed, and these correspond to a locking of the breather frequency to a particular cavity mode frequency. These resonances allow us to use the tunable roto-breather as a spectroscopic tool to study the properties of cavity modes in a JJL.

The strong interaction of breathers with cavity modes in JJLs leads to the possibility of studying resonant scattering of cavity modes by roto-breathers [39]. Again, the dissipation helps in stabilizing the breather during the scattering process. The transmission for plasmons is strongly dependent upon their wave numbers. In addition, strong resonances can be obtained in the scattering, ranging from resonant transmission to resonant reflection. By changing the d.c. bias, the roto-breather is changed, and thus so is the scattering potential. Consequently, roto-breathers may serve as tunable frequency filters for plasmon waves in the 100 GHz frequency domain.

Another consequence of the presence of dissipation is the possibility of exciting genuine quasi-periodic breathers. This has been achieved, both theoretically and experimentally, by using the fact that not all resistive junctions have to lock to the cavity mode when a breather is driven into a resonance [40]. In such a case, the breather becomes an object where different resistive junctions rotate at various incommensurate frequencies. Due to the interaction, the final state is quasi-periodic in time.

3.1.3 Laser Scanning Microscopy

The technique of laser scanning microscopy finally allowed visualization of the experimentally obtained breather states [37]. To do this, the ladder is prepared in a given state, and the voltage drop across the ladder is monitored. Then, the probe is scanned with a laser beam with a moderate intensity and a cross-section diameter of few micrometres. The laser beam locally heats the probe. If it hits a resistive junction, the local temperature change will induce a change of the junction characteristics, and finally a change in the measured voltage drop. Otherwise, the voltage drop will show no response. In Fig. 12, the outcome of such experiments and the corresponding schematics are shown for the case of annular ladders. Both delocalized resistive states and roto-breather states are clearly visible. In the schematics, Josephson junctions (each about $3\mu\text{m}$ wide) lie at the mid-points of each of the line segments that signify superconducting leads connecting the junctions. A homogeneous ladder in the schematic and a homogeneous background in the data would signal a superconducting state of all junctions at low d.c. current, i.e. the linear regime. However, a large d.c. current switches some of the junctions into a resistive state that supports a voltage across the junctions; in the schematic, dots depict resistive junctions having different voltages. The resistive junctions belong to discrete breather excitations localized at various sites of the ladder.

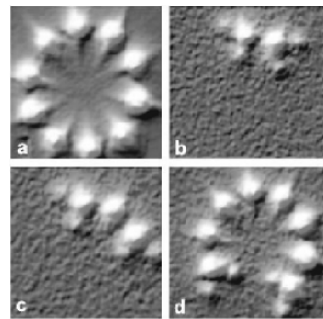
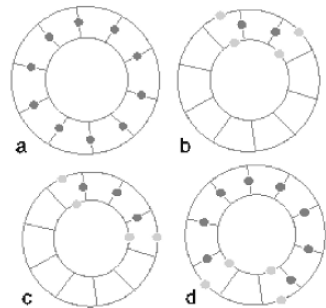


Fig. 12 Experimental and schematic images of roto-breathers in an annular Josephson ladder driven by a d.c. current. Among the many possible DB states, the data show four: (a) a highly excited, spatially homogeneous resistive state and (b–d) localized states corresponding to several distinct DBs (Figure adapted from [41])



3.2 Coupled Nonlinear Optical Waveguides and Resonators

Another experimental set-up used to observe discrete breathers is associated with coupled optical waveguides, which form periodic structures in one and two dimensions [42, 43, 44]. These structures represent generalizations of the nonlinear optical coupler, introduced by Jensen [45]. There are generally two different approaches to the experimental realization of coupled waveguide arrays. One is the etching of fixed waveguides in nonlinear materials, such as semiconductors [46], and the other is induction of periodic structures in compliant media, such as optical induction in photorefractive crystals [43] or periodic voltage biasing in liquid crystals [47]. Figures 13 and 14 illustrate typical one- and two-dimensional waveguide arrays produced by each of the two methods.

3.2.1 Basic Principles and Modelling

The standard theoretical approach for studying light propagation in waveguide arrays is based on the concept of coupled waveguide modes – see Fig 13(b) – which is similar to the tight-binding approximation used in solid state theory. Typical propagation distances in waveguide arrays are rather short, so that the effects of dispersion and diffraction in each individual waveguide are usually neglected.¹ With this assumption, and also only considering Kerr-type nonlinearity, the corresponding set of equations for the amplitudes of the waveguide modes, E_n , reduces to the DNLS model [44]:

$$i \frac{dE_n}{dz} + \beta E_n + C(E_{n-1} + E_{n+1}) + \gamma |E_n|^2 E_n = 0, \quad (45)$$

where β is the linear propagation constant (taken to be the same in each waveguide), C is the coupling coefficient between adjacent waveguide modes, and γ is the

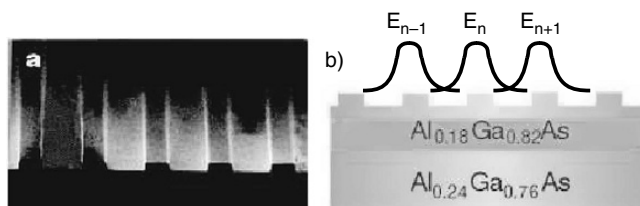


Fig. 13 A one-dimensional AlGaAs waveguide array. It is composed of three layers of AlGaAs material: the substrate and cladding with a lower refractive index and the guiding layer with the higher refractive index. Periodic etching of the cladding forms coupled waveguides. (a) A snapshot of the waveguide array. (b) Schematic structure of the waveguide array with illustration of modal overlap (Figure adapted from [42])

¹ Glass- and semiconductor-based waveguide arrays usually require picosecond or sub-picosecond pulsed lasers in order to achieve high-enough intensities for a nonlinear response. This can introduce spatio-temporal effects [48].

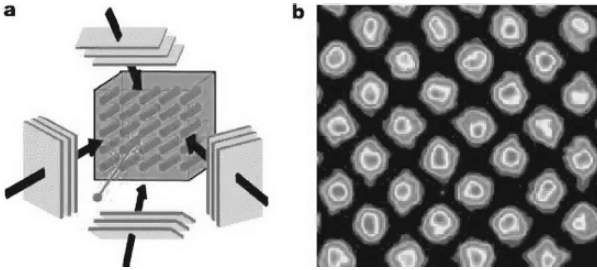


Fig. 14 (a) Diagram of an experimental set-up for observing two-dimensional discrete localized structures with the use of a photorefractive crystal – two interfering pairs of ordinarily polarized plane waves induce the photonic array, while the extraordinarily polarized probe beam is focused into a single waveguide and eventually forms a discrete soliton. (b) Typical observation of a waveguide array at the exit face of the crystal for low-probe beam power (no soliton formation). Each waveguide is approximately $7\mu\text{m}$ in diameter, with an $11\mu\text{m}$ spacing between nearest neighbours (Figure adapted from [52])

nonlinear parameter [49, 50, 44]. To the lowest-order approximation, only coupling between nearest neighbours is taken into account, while nonlinear coupling terms are neglected. For waveguide arrays created by optical induction in photorefractive materials [43], the nonlinear term in (45) is usually modified to account for saturation effects, and then takes the form $\gamma E_n / (1 + |E_n|^2)$ [51]. Generalization to higher-dimensional problems is straightforward, cf. (18). In the above model, the actual evolution coordinate is the propagation distance z , which plays the role of an effective time. For that reason, we will refer to wave propagation constants along the z -axis as spatial frequencies, in analogy with other discrete models introduced earlier.

3.2.2 Discrete Solitons: Stationary DBs in One- and Two-Dimensional Coupled Waveguide Structures

The DNLS model (45) represents a very specific type of discrete nonlinear system which supports time-periodic solutions (space periodic in the z coordinate) where only one frequency is excited:

$$E_n(z) = A_n \exp(-i\Omega_b z). \quad (46)$$

Using a suitable rescaling of spatial frequencies Ω_b , the propagation constant β in (45) can be set to zero without loss of generality. Figures 15 and 16 illustrate basic types of stationary DBs in one- and two-dimensional DNLS models, while experimentally observed localized excitations in the corresponding waveguide array set-ups are presented in Fig. 17. Due to the stationary character of such excitations, they are often referred to as *discrete solitons*, rather than breathers.

The DNLS model is used as a convenient playground for analysing basic nonlinear phenomena because of its relative simplicity. On the other hand, DNLS

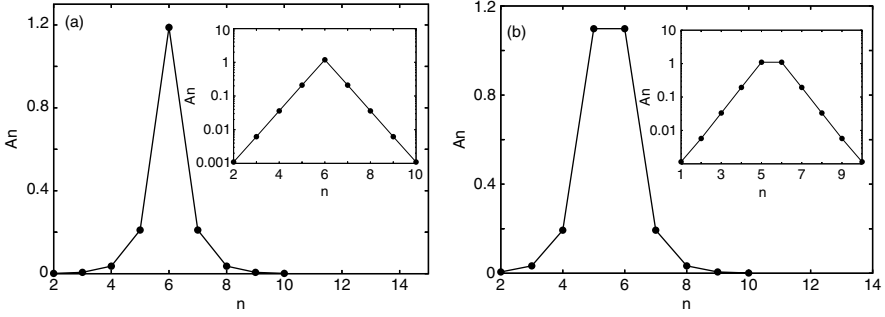


Fig. 15 Profiles of single-site (a) and two-site (b) stationary DB solutions (46) of the one-dimensional DNLS model, (45), using normal and log-normal (insets) plots. Parameter values are $\Omega_b = 1.0, C = 0.25, \gamma = 1$. Lines are to help visualization

equations can be derived as approximate small-amplitude models of more general nonlinear lattice models with on-site nonlinear potential (Klein–Gordon lattices) [5, 53, 54, 55, 56], inter-site nonlinear interaction (Fermi–Pasta–Ulam lattices) [57, 58, 59], and mixed-type nonlinearities [60]. One essentially uses the rotating wave approximation (RWA), which neglects the effect of the generation of higher harmonics. In this respect, coupled optical waveguides provide one with effective tools to test numerous theoretical predictions.

One of the obvious advantages of using optical waveguide arrays, as compared to many other experimental realizations of DBs, is that no special technique is needed to observe the localized states that are obtained. A snapshot, taken with a

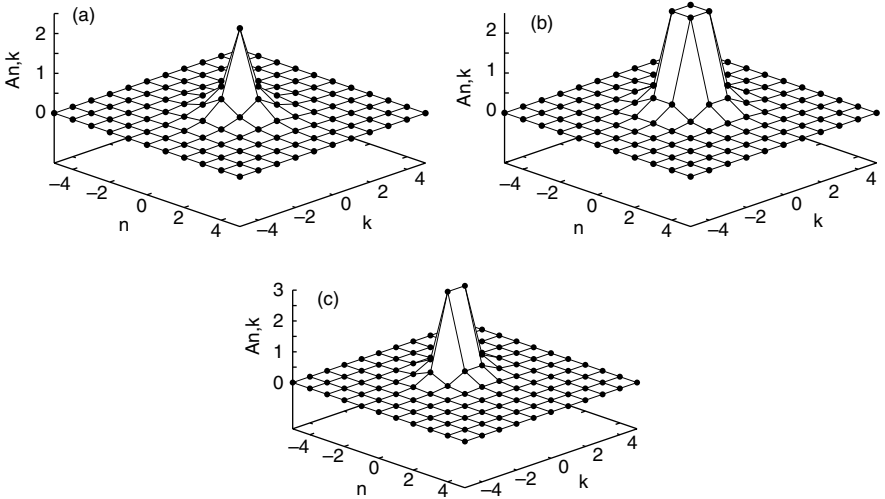


Fig. 16 Different types of DBs in the two-dimensional DNLS model with $\gamma = 1$ and $C = 4$: (a) single-site DB, $\Omega_b = 5.5$; (b) inter-site DB, $\Omega_b = 8$; (c) ‘hybrid’-type DB, $\Omega_b = 9$

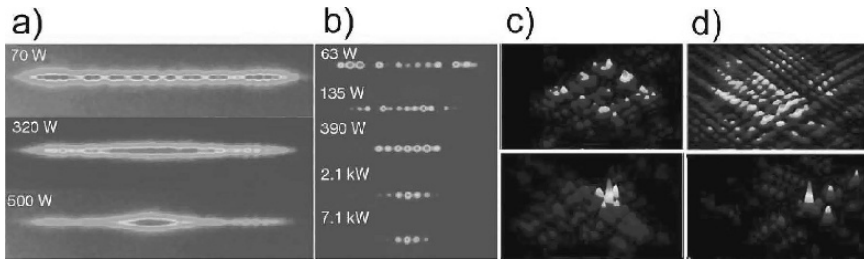


Fig. 17 Experimental observation of discrete diffraction in the linear regime (small input power) and localization in the nonlinear regime (high input power). **(a)** Experimental images of a Kerr-type AlGaAs one-dimensional waveguide array with waveguide spacing $D = 8 \mu\text{m}$, operated at a wavelength of $\lambda = 1.53 \mu\text{m}$ [61]. **(b)** The same for a periodically poled lithium niobate array with $D = 15 \mu\text{m}$, operated at a wavelength of $\lambda = 1.56 \mu\text{m}$ [42]. **(c)** and **(d)** The same for a two-dimensional optically induced waveguide array, shown in Fig. 14, with the input beam at normal incidence and at an angle of 0.55° to the lattice plane (at the edge of the first Brillouin zone), respectively. The signs of the voltage applied to the photorefractive crystal in **(c)** and **(d)** are opposite, corresponding to focusing and defocusing nonlinearities, respectively (Figure adapted from [52])

high-resolution infrared camera at the output facet of the array, provides full information about the light intensity distribution among the coupled waveguides. In addition, optical set-ups provide a unique opportunity for observing the actual dynamics of a discrete system by monitoring the light intensity evolution along the propagation direction. For example, this can be done by scanning the evanescent light from the top of the waveguide array [62]. As a result, the formation of various types of one- and two-dimensional DBs has been successfully observed in optical experiments, and, additionally, different intriguing aspects of the DB dynamics have been tested. In particular, interactions between highly localized discrete solitons and propagating broad wave packets have recently been observed experimentally in AlGaAs waveguide arrays [63, 64]. Also, possible experimental set-ups for the direct observation of resonant linear wave scattering by DBs and associated spectral hole-burning effects have been developed on the basis of optical waveguides [65, 66].

We also note that DNLS models can support more general types of time-periodic solutions, with several harmonics excited [6, 67, 68, 69]. Similar optical breathers were recently observed experimentally [70].

3.2.3 Coupled Resonators

A closely related and intensively developing subfield of nonlinear optics deals with coupled optical resonators. A straightforward generalization of the above waveguide array set-ups is given by a set of coupled zero-dimensional resonators [71], where mirrors are applied to the input and output facets of the array – see Fig. 18(a). Other possible set-ups include periodically arranged defect cavities in photonic crystals and coupled micro-ring resonators – see Fig. 18(b) and (c), respectively.

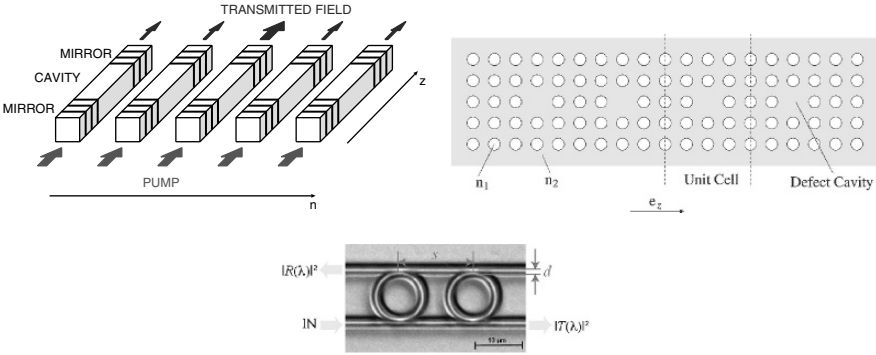


Fig. 18 Different set-ups of coupled optical resonators. *Top left*: coupled semiconductor resonators with mirrors applied at the input and output facets of waveguides (After [71]). *Top right*: periodically arranged defect cavities in a photonic crystal (After [72]). *Bottom*: coupled micro-ring resonators (After [73])

The corresponding theoretical models should account for dissipation, which is one of the principal ingredients in any resonator system. One of the simplest models is given by the driven and damped DNLS system [71], in which dissipative terms are taken to be linear in the field amplitude:

$$\left(i \frac{\partial}{\partial \tau} + \Delta + i + \gamma |E_n|^2 \right) E_n + C(E_{n+1} + E_{n-1} - 2E_n) = A_n^{(\text{in})}. \quad (47)$$

Here, τ is the effective evolution coordinate, E_n is the field amplitude in the n th resonator, C is the coupling between adjacent resonators, Δ is the detuning from linear resonance, γ is the nonlinear Kerr coefficient, and the damping term is rescaled to unity. The amplitudes $A_n^{(\text{in})}$ originate from the input field (pump), which can be non-homogeneous across the array.

In the case of a homogeneous pump, $A_n^{(\text{in})} = \text{const.}$, (47) supports different types of bright and dark stationary DBs – see Fig. 19. Due to dissipation, these objects no longer form families of solutions, but correspond to attractors in phase space. All the characteristics of such DBs, including their amplitude and phase, are fully determined by the model parameters and the parameters of the pump (its amplitude and phase). To a certain extent, this makes the dynamics of the driven-damped DNLS less rich than that of its Hamiltonian analogue. However, dissipation also brings certain new features to the dynamics of localized excitations. It can suppress some resonances with extended states of the system, which otherwise do not allow for quasi-periodic and moving DBs. Earlier, we mentioned the observation of quasi-periodic DBs in coupled Josephson junction systems. Here we will focus on moving DBs.

A tilted pump, $A_n^{(\text{in})} = a \exp(i\phi_{\text{in}} n)$, which corresponds, for example, to an inclination of the incidence field in the set-up of Fig. 18(a), induces a transverse force acting on a DB. This, in turn, can cause the DB to move across the array – see

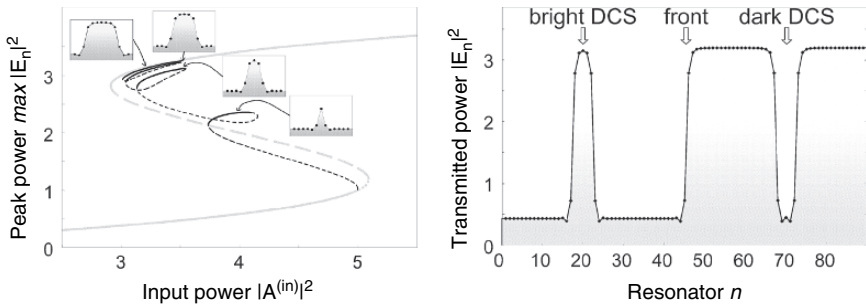


Fig. 19 *Left*: bifurcation diagram for the bistable homogeneous ground state of (47) (grey lines), and different types of bright stationary DBs (black lines). Solid curves indicate stable solutions, while dashed curves indicate unstable ones. Parameter values are $\gamma = 1$, $\Delta = -3$, $C = 0.25$. *Right*: co-existence of different types of stationary DBs. Parameter values are $\gamma = -1$, $\Delta = 3$, $C = 0.25$, $|A^{(in)}|^2 = 3.3$ (Figure adapted from [71])

Fig. 20 Average velocity of a DB (W/h) versus normalized tilt (V_0/h) for various coupling constants. The inset illustrates the position of the centre of moving DBs for various tilts (Figure adapted from [74])

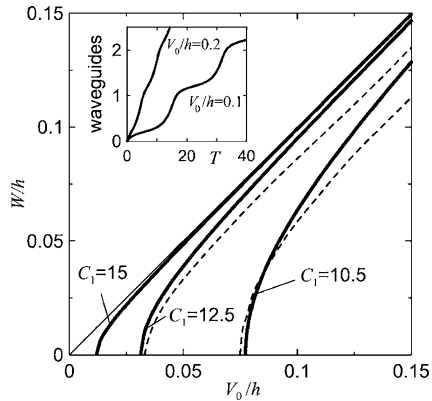


Fig. 20. It is important that the discreteness of the system hinders such motion and, in some cases, even prevents it [74]. Generally, there exists a critical value of the tilt, $\phi_{in}^{(cr)}$, below which a given type of DB cannot move – see Fig. 20. This is in contrast to continuous systems, where the resulting velocity of a cavity soliton is linearly proportional to the tilt [75].

The inherent nonlinearity of the DB velocity as a function of the tilt, $V(\phi_{in})$, in the vicinity of the critical point, $\phi_{in}^{(cr)}$, gives rise to the effect of DB ratchet motion under the influence of a periodically changing tilt with zero average value [76] – see Fig. 21. A necessary condition for the observation of such a DB ratchet effect is the violation of certain symmetries of the system, and this can be achieved, for example, by applying a bi-harmonic variation of the tilt, or by a superposition of two pumps with varying tilts at different frequencies [76]. For adiabatically changing tilt(s), the average velocity of the resulting net motion of a DB can be estimated to be

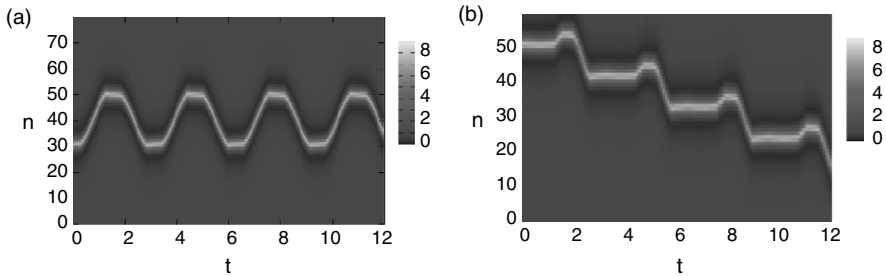


Fig. 21 Density plots of $|E_n|^2$ for DB motion under a periodically changing tilt of the input field. **(a)** Periodic motion of a DB under the influence of a single-harmonic periodically changing tilt. **(b)** Ratchet motion of a DB under the influence of superimposed pumps with varying tilts at different frequencies (Figure adapted from [76])

$\bar{V} = \frac{1}{T} \int_0^T V[\phi_{\text{in}}(\tau)] d\tau$, where T is the period of the tilt. Obviously, the ratchet effect vanishes in the continuous limit, where the function $V(\phi_{\text{in}})$ becomes linear.

3.3 Other Examples

Dissipation is unavoidable in any experiment. Nevertheless, it is characterized by some time scale, and experiments which probe a system on shorter time scales are not influenced by the dissipation. In the above examples, the experimental time scales were much larger than the dissipation time scale, so the properties of the discrete breathers were strongly influenced by it. Let us briefly mention two more examples, from recent studies, which fall into this category.

Sato, Hubbard, and Sievers studied the generation of breathers in driven micro-mechanical cantilever arrays [77]. The frequency of the a.c. drive is chosen to be close to the linear cavity mode spectrum, but not resonant with it. Discrete breathers are spontaneously generated and stabilized by the a.c. drive. Once a DB is generated, laser beams are used to guide it along the cantilever lattice.

Sato and Sievers performed several experiments with anti-ferromagnets. A sophisticated set of different electromagnetic pulses are used to excite localized spin excitations [78]. Further pulses are used to stabilize DBs and finally to observe their decay in a controlled way. Although they are indirect, these experiments are an impressive example of controlling the excitation and properties of DBs at nanometre scales.

4 Summary

The rapidly growing field of the theory and applications of discrete breather excitations is too large to be covered in one chapter. As we pointed out here, a subclass of experimental studies makes a focus on the particular case of nonlinearity,

discreteness, and dissipation. While dissipation is not crucial here for the mere existence of DBs, it has a profound impact on many of their properties. A DB can be brought into resonance with cavity modes, without destroying the DB itself. Also DBs can become quasi-periodic in time, which again, in general, is impossible in the absence of dissipation. DBs can start to move along the lattice, in contrast to the case without dissipation. Finally, control over the strength of dissipation naturally introduces new, and sometimes easily accessible, control parameters which can be used in experiments.

References

1. A.A. Ovchinnikov, Zh. Eksp. Teor. Fiz. / Sov. Phys. JETP **57** / **30**, 263/147 (1969/1970).
2. A.J. Sievers and S. Takeno, Phys. Rev. Lett. **61**, 970 (1988).
3. S. Takeno and A. Sievers, Solid State Commun. **67**, 1023 (1988).
4. S. Takeno, K. Kisoda, and A. J. Sievers, Prog. Theor. Phys. Suppl. **94**, 242 (1988).
5. S. Flach and C. R. Willis, Phys. Rep. **295**, 182 (1998).
6. R.S. MacKay and S. Aubry, Nonlinearity **7**, 1623 (1994).
7. S. Flach, Phys. Rev. E **50**, 3134 (1994).
8. S. Aubry and T. Cretegny, Physica D **119**, 34 (1998).
9. S. Flach and K. Kladko, Physica D **127**, 61 (1999).
10. D. Campbell, S. Flach, and Y. Kivshar, Phys. Today **57**, 43 (2004).
11. S. Flach and A. Gorbach, Chaos **15**, 015112 (2005).
12. M. Eleftheriou and S. Flach, Physica D **202**, 142 (2005).
13. E.N. Economou, *Green's Functions in Quantum Physics*, (Springer-Verlag, Berlin, 1990).
14. C. Baesens and R. S. MacKay, Nonlinearity **10**, 931 (1997).
15. A. Zygmund, *Trigonometric Series*, (Cambridge University Press, Cambridge, 1968).
16. S. Flach, Phys. Rev. E **51**, 3579 (1995).
17. S. Flach, K. Kladko, and R. S. MacKay, Phys. Rev. Lett. **78**, 1207 (1997).
18. S. Flach, Phys. Rev. E **58**, R4116 (1998).
19. Y.S. Kivshar, Phys. Rev. E **48**, R43 (1993).
20. F. Fischer, Ann. Physik **2**, 296 (1993).
21. S. Flach, Phys. Rev. E **51**, 1503 (1995).
22. J. L. Marín and S. Aubry, Nonlinearity **9**, 1501 (1996).
23. A. A. Ovchinnikov and S. Flach, Phys. Rev. Lett. **83**, 248 (1999).
24. B. Dey, M. Eleftheriou, S. Flach, and G.P. Tsironis, Phys. Rev. E **65**, 017601 (2001).
25. A. Gorbach and S. Flach, Phys. Rev. E **72**, 056607 (2005).
26. S. Flach, K. Kladko, and S. Takeno, Phys. Rev. Lett. **79**, 4838 (1997).
27. S. Aubry, Physica D **103**, 201 (1997).
28. J.L. Marín and S. Aubry, Physica D **119**, 163 (1998).
29. V.I. Arnold, *Mathematical Methods of Classical Mechanics*, (Springer-Verlag, New York, 1989), 2nd ed.
30. A.H. Nayfeh, *Introduction to Perturbation Techniques*, (John Wiley and Sons, New York, 1993).
31. S. Flach, Physica **D91**, 223 (1996).
32. M. I. Weinstein, Nonlinearity **12**, 673 (1999).
33. L. M. Floría, J. L. Marín, P. J. Martínez, F. Falo, and S. Aubry, Europhys. Lett. **36**, 539 (1996).
34. J.L. Marín, F. Falo, P.J. Martínez, and L.M. Floría, Phys. Rev. E **63**, 066603 (2001).
35. S. Takeno and M. Peyrard, Phys. Rev. E **55**, 1922 (1997).
36. A. Miroshnichenko, S. Flach, M. Fistul, Y. Zolotaryuk, and J.B. Page, Phys. Rev. E **64**, 066601 (2001).
37. P. Binder, D. Abraimov, A.V. Ustinov, S. Flach, and Y. Zolotaryuk, Phys. Rev. Lett. **84**, 745 (2000).
38. E. Trias, J.J. Mazo, and T. Orlando, Phys. Rev. Lett. **84**, 741 (2000).
39. A.E. Miroshnichenko, M. Schuster, S. Flach, M.V. Fistul, and A.V. Ustinov, Phys. Rev. B **71**, 174306 (2005).

40. M.V. Fistul, A.E. Miroshnichenko, S. Flach, M. Schuster, and A.V. Ustinov, *Phys. Rev. B* **65**, 174524 (2002).
41. A.V. Ustinov, *Chaos* **13**, 716 (2003).
42. D.N. Christodoulides, F. Lederer, and Y. Silberberg, *Nature* **424**, 817 (2003).
43. J.W. Fleischer, G. Bartal, O. Cohen, T. Schwartz, O. Manela, B. Freedman, M. Segev, H. Buljan, and N.K. Efremidis, *Opt. Express* **13**, 1780 (2005).
44. Y.S. Kivshar and G.P. Agrawal, *Optical Solitons: From Fibers to Photonic Crystals*, (Elsevier Science, Amsterdam, 2003).
45. S.M. Jensen, *IEEE J. Quant. Electronics* **18**, 1580 (1982).
46. P. Millar, J.S. Aitchison, J.U. Kang, G.I. Stegeman, A. Villeneuve, G.T. Kennedy, and W. Sibbett, *J. Opt. Soc. Am. B* **14**, 3224 (1997).
47. A. Fratallocchi, G. Assanto, K.A. Brzdakiewicz, and M.A. Karpierz, *Opt. Lett.* **29**, 1530 (2004).
48. D. Cheskis, S. Bar-Ad, R. Morandotti, J.S. Aitchison, H.S. Eisenberg, Y. Silberberg, and D. Ross, *Phys. Rev. Lett.* **91**, 223901 (pages 4) (2003).
49. D.N. Christodoulides and R.I. Joseph, *Opt. Lett.* **13**, 794 (1988).
50. M.J. Ablowitz and Z.H. Musslimani, *Physica D: Nonl. Phen.* **184**, 276 (2003).
51. M. Stepic, D. Kip, L. Hadzievski, and A. Maluckov, *Phys. Rev. E* **69**, 066618 (2004).
52. J. Fleischer, M. Segev, N. Efremidis, and D. Christodoulides, *Nature* **422**, 147 (2003).
53. A. Morgante, M. Johansson, G. Kopidakis, and S. Aubry, *Physica D* **162**, 5394 (2002).
54. I. Daumont, T. Dauxois, and M. Peyrard, *Nonlinearity* **10**, 617 (1997).
55. Y.S. Kivshar and M. Peyrard, *Phys. Rev. A* **46**, 3198 (1992).
56. Y.S. Kivshar, *Phys. Lett. A* **173**, 172 (1993).
57. V.M. Burlakov, S.A. Kisilev, and V.I. Rupasov, *JETP Lett.* **51**, 544 (1990).
58. C. Claude, Y.S. Kivshar, O. Kluth, and K.H. Spatschek, *Phys. Rev. B* **47**, 14228 (1993).
59. Y. Kivshar, *Phys. Rev. E* **48**, 4132 (1993).
60. M. Johansson, *Physica D* **216**, 62 (2006).
61. H.S. Eisenberg, Y. Silberberg, R. Morandotti, A.R. Boyd, and J.S. Aitchison, *Phys. Rev. Lett.* **81**, 3383 (1998).
62. Y. Linzon, I. Ilisar, D. Cheskis, R. Morandotti, J.S. Aitchison, and S. Bar-Ad, *Phys. Rev. E* **72**, 066607 (2005).
63. J. Meier, G.I. Stegeman, D.N. Christodoulides, Y. Silberberg, R. Morandotti, H. Yang, G. Salamo, M. Sorel, and J.S. Aitchison, *Opt. Lett.* **30**, 1027 (2005).
64. J. Meier, G.I. Stegeman, D.N. Christodoulides, R. Morandotti, G. Salamo, H. Yang, M. Sorel, Y. Silberberg, and J.S. Aitchison, *Opt. Lett.* **30**, 3174 (2005).
65. S. Flach, V. Fleurov, A.V. Gorbach, and A.E. Miroshnichenko, *Phys. Rev. Lett.* **95**, 023901 (2005).
66. A. Gorbach, V. Fleurov, S. Flach, and A. Miroshnichenko, in *Topical Problems of Nonlinear Wave Physics*, edited by A. Sergeev, (Proceedings of SPIE, Bellingham, 2006), Vol. **5975**, pp. 297–306.
67. M. Johansson, S. Aubry, Y.B. Gaididei, P.L. Christiansen, and K.O. Rasmussen, *Physica D* **119**, 115 (1998).
68. M. Johansson and S. Aubry, *Nonlinearity* **10**, 1151 (1997).
69. M. Johansson and A. V. Gorbach, *Phys. Rev. E* **70**, 057604 (2004).
70. D. Mandelik, H.S. Eisenberg, Y. Silberberg, R. Morandotti, and J.S. Aitchison, *Phys. Rev. Lett.* **90**, 253902 (2003).
71. U. Peschel, O. Egorov, and F. Lederer, *Opt. Lett.* **29**, 1909 (2004).
72. A. Yariv, Y. Xu, R.K. Lee, and A. Scherer, *Opt. Lett.* **24**, 711 (1999).
73. Q. Xu, S. Sandhu, M.L. Povinelli, J. Shakya, S. Fan, and M. Lipson, *Phys. Rev. Lett.* **96**, 123901 (2006).
74. O. Egorov, U. Peschel, and F. Lederer, *Phys. Rev. E* **72**, 066603 (2005).
75. S. Fedorov, D. Michaelis, U. Peschel, C. Etrich, D.V. Skryabin, N. Rosanov, and F. Lederer, *Phys. Rev. E* **64**, 036610 (2001).
76. A. Gorbach, S. Denisov, and S. Flach, *Opt. Lett.* **31**, 1702 (2006).
77. M. Sato, B.E. Hubbard, and A.J. Sievers, *Rev. Mod. Phys.* **78**, 137 (2006).
78. M. Sato and A.J. Sievers, *Nature* **432**, 486 (2004).